LIMNOLOGY
and
OCEANOGRAPHY

ASLO

*Limnol. Oceanogr.* 64, 2019, 1252–1269

doi: 10.1002/lno.11111

# Tracking Lagrangian transport in Lake Geneva: A 3D numerical modeling investigation

**A. A. Cimatoribus**,* **U. Lemmin, D. A. Barry**
Ecological Engineering Laboratory (ECOL), Institute of Environmental Engineering (IIE), School of Architecture, Civil and Environmental Engineering (ENAC), École Polytechnique Fédérale de Lausanne (EPFL), Lausanne, Switzerland

## *Abstract*

Lake Geneva, the largest freshwater lake in Western Europe, is subject to important environmental pressures from its densely populated shores and watershed. To maintain and improve water quality in this lake, as well as in other enclosed or semi-enclosed basins, it is essential to understand and be able to predict how nutrients and pollutants are transported within it. A 3D numerical modeling study of Lagrangian transport in Lake Geneva is presented, showing the dispersion of water (based on tracking inert water particles) inflowing from the lake's main tributary, the Rhône River. The relation between dominant winds, circulation patterns, and transport was analyzed. The results demonstrated that transport within the lake is highly inhomogeneous in space and intermittent in time, because water mass movements are controlled by the wind-induced formation of large-scale gyres and their subsequent breakdown into smaller ones. Particle spreading was shown to be sensitive to the depth of the initial particle release, and to the mean depth of the particles' trajectory. However, several preferential pathways could be identified. Some water particles rapidly (days) traveled across the entire lake, through the near-shore region in the upper layer, while others remained trapped for months, particularly in the central region of the lake at depth. Deeper particles tended to remain longer in the lake, due to the insulating effect of stratification, bathymetry obstacles, and slower currents at greater depth.

Understanding how river inflow is transported within an enclosed or semi-enclosed water body is essential for effective water resource management. Dispersion pathways determine the fate of nutrients and pollutants carried by inflowing waters, affect water renewal, and can severely impact oxygen availability. Even in the presence of large inflows and outflows, water residence times can widely vary (Monsen et al. 2002). In this paper, a numerical study of Lagrangian transport was carried out in Lake Geneva (local name: Lac Léman). Lake Geneva is the largest lake in Western Europe. It is located between Switzerland and France, and is surrounded by the Alps to the south and east, and by the Jura chain to the northwest. Lake Geneva has a surface area of approximately 580 $km^2$, a major axis of 72 km and a maximum width of 14 km. The lake is composed of two basins: the narrow shallow *Petit Lac* to the west, and the wide deep *Grand Lac* to the east (Fig. 1).

The main river inflow is the Rhône River, entering at the lake's eastern end with a mean inflow rate of 182 $m^3\ s^{-1}$ (CIPEL 2017). The mean outflow (Rhône River; 250 $m^3\ s^{-1}$; *see* Fig. 1) at the western end of the lake is controlled with a gate that maintains the lake level nearly constant. Smaller rivers and precipitation contribute the difference between the Rhône River inflow and outflow. The maximum depth of the lake is 309 m and the mean depth is 172 m, with a total volume of approximately 89 $km^3$. This large volume and relatively small river throughflow lead to a long flushing time (also referred to as "theoretical residence time" in the literature) of approximately 11 yr (CIPEL 2017), with the flushing time being the ratio of mean volume to outflow (Monsen et al. 2002). Temperature gradients maintain vertical density stratification year-round, with occasional deep mixing during particularly cold winters. Coriolis force effects are important in the momentum balance; The inertial period at the latitude of Lake Geneva is approximately 16.5 h.

Water circulation in Lake Geneva is mainly forced by wind. The strongest winds are the "Vent," coming from the southwest, and the "Bise," coming from the northeast (Fig. 1). The spatial variability of wind above the lake is mainly determined

*Correspondence: andrea.cimatoribus@epfl.ch



Additional Supporting Information may be found in the online version of this article.

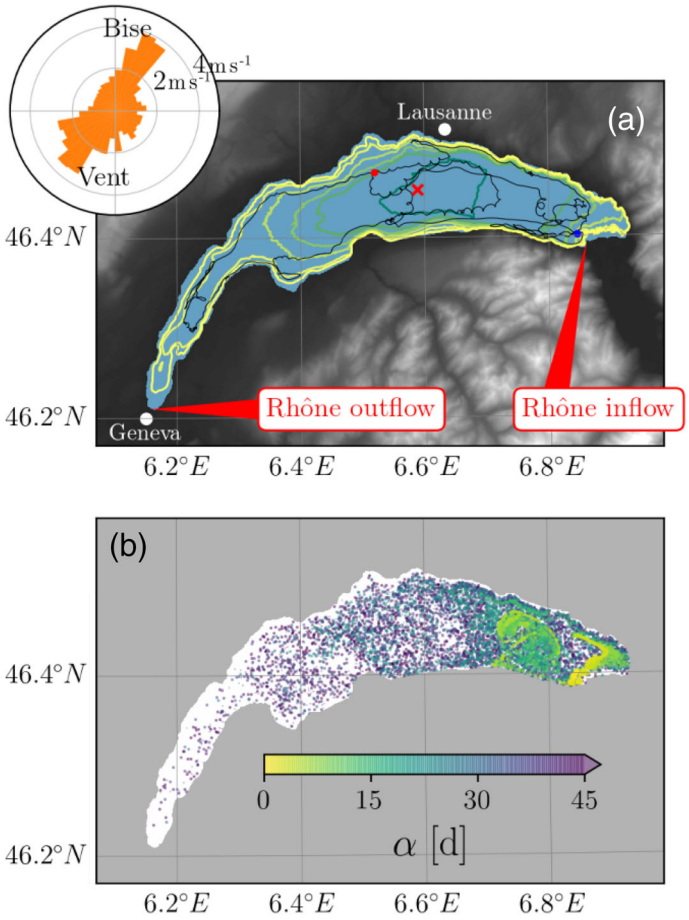


**Fig. 1.** (**a**) Map of Lake Geneva and its surrounding area. Colored isobath contours mark the depths of 25, 50, 100, 150, 200, and 300 m (yellow: shallow waters; green: deep). The topographic elevation of the surrounding areas is shaded (lighter: higher). Locations of the Rhône River inflow and outflow, and the two largest cities, Lausanne and Geneva, are indicated. The trajectory of a particle from the summer simulation *SG* is overlaid (black line), with start (blue dot) and end points (red dot). The red cross marks the SHL2 field station, in the deepest part of the lake. The circular upper left inset gives the mean wind speed (in m $s^{-1}$) over the lake as a function of the direction; winds from the northeast (Bise) and southwest (Vent) are relatively more frequent. (**b**) Snapshot from simulation *YG* on 08 February 2016 at 12:30. The position of the particles that were released up to this time at a depth of 20 m is shown, colored according to their age (*see* color bar).

by topography, with the eastern end of the lake being more sheltered (Lemmin and D'Adamo 1997). The large-scale response of the lake to wind forcing was previously described as a combination of Kelvin and near-inertial standing internal waves (Bauer et al. 1981; Bäuerle 1985; Lemmin et al. 2005). Dominant internal Kelvin modes were identified at periods of 80, 55, and 33 h, while near-inertial and Poincaré modes were observed at periods shorter than the inertial one (16.5 h).

The Lake Geneva region hosts a population of over 1 million and major agricultural and industrial activities that all depend on the lake as an essential freshwater resource (CIPEL 2017). As the main river inflow, the Rhône River, is the strongest driver of water renewal in the basin, tracking the dispersion of its water within the lake is important for effective lake water management. The Rhône River inflow is also a significant contributor to the sediment input into the lake (Giovanoli 1990; Loizeau et al. 2012). Its plume can sink directly to the bottom during short, episodic high-discharge events (underflow), when the river brings in the largest load of solid material. More common are interflows, which carry only finer sediments, when the river plume is not sufficiently dense to reach the bottom. Interflows detach from the bottom at the neutral buoyancy depth, most often around the thermocline level. The interflow is subsequently transported by the general lake circulation and its signature can be identified in the water column from conductivity–temperature–depth profiling (Ishiguro 2004), as well as in the sediments (Dominik et al. 1983; Vernet and Viel 1984; Giovanoli 1990; Loizeau et al. 2017) for tens of kilometers from the river mouth. These studies indicate that the Rhône River plume is most often detected along the northern shore, due to the Coriolis force effect on the interflow. Loizeau (pers. comm.) observed that the fine particles that characterize the sediments of Rhône River origin are more abundant along the northern near-shore region than in the rest of the lake.

By measuring the stable hydrogen and oxygen isotope composition of the water, Halder et al. (2013) inferred the fraction of water originating from the Rhône River throughout the lake. The Rhône River water signature was stronger in summer and was located just above the thermocline (roughly 20 m depth), consistent with the spreading as an interflow. Their results also suggested that mixing of the river water is slow in the interflow. Furthermore, they implied that a water parcel could move from the Rhône River mouth to the *Petit Lac* (50 km) in less than about 5 months during spring and summer, identifying an upper limit for the minimum residence time between the Rhône River mouth and the *Petit Lac*. Here, "residence time" indicates the time it takes for a water parcel to travel from its initial position to a given area (Monsen et al. 2002).

Mercanton (1932) traced the trajectories of freely drifting fishing nets and observed that they often followed shore-parallel trajectories when released not too far from the shore. Occasionally, however, they moved into the central region of the lake and even crossed the lake within one night. As will be shown below, these patterns relate to the dynamics of shore-parallel currents in the near-shore region and large-scale gyres in the central region of the lake. Umlauf and Lemmin (2005) demonstrated the importance of wind-excited Kelvin waves for driving exchanges between the *Petit Lac* and *Grand Lac* and showed that both Vent and Bise winds are capable of triggering the exchange of large portions of the hypolimnetic waters of these basins, on time scales of a few days. Other studies examined the spreading of pollutants from a water treatment outfall located in a bay in the northern part of Lake Geneva

(Goldscheider et al. 2007; Bonvin et al. 2011; Razmi et al. 2014). They concluded that pollutant dispersion is sensitive to local wind and mean flow conditions, and that water recirculation within the bay can prevent the spreading of pollutants for up to several days.

Here, Lagrangian transport in Lake Geneva is investigated numerically by tracking the three-dimensional (3D) Lagrangian motion of particles that have neither mass nor volume. Therefore, they do not affect water density and are passively advected by the velocity field obtained with a hydrodynamic model of the whole lake (Cimatoribus et al. 2018). These numerical particles can be seen as markers of individual water parcels. In the field, comparable information could be obtained by following the mean trajectory of a patch of water marked with a tracer. Our focus was on water originating from the Rhône River. It should be noted that realistically representing the near-field dynamics of the river entering the lake within a numerical model is a challenging effort, and doing so within a basin-scale model is computationally impossible. For this reason, we instead investigated how transport properties depend on the initial depth of release near the river mouth. Studying the dispersion of passive tracers within the flow field computed by the hydrodynamic model would provide a largely equivalent perspective on transport in the lake. However, concentrating on particles allowed investigating age and residence time, which in turn highlighted preferred passageways and relatively stagnant regions of the lake. Furthermore, the use of particles avoids the need to calibrate a turbulence model for tracers, which would currently be infeasible due to the lack of field data.

The paper is organized as follows. The Methods section describes the 3D hydrodynamic numerical model, the particle-tracking algorithm, and the data analysis methods used. In the Results section, hydrodynamic model results are analyzed to determine residence time and age distribution, as well as the effects of wind forcing on the trajectories. The Discussion and conclusions section then follows. As a visual complement, the Supporting Information (SI) includes three animations obtained from the particle simulations.

## Methods

In this section, the numerical modeling tools applied in this study are presented. A 3D hydrodynamic model was used to compute the velocity field, which served as the basis for the particle tracking simulations.

### Hydrodynamic model

The hydrodynamic model is based on the MITgcm code (Marshall et al. 1997), which solves the 3D Boussinesq, hydrostatic Navier–Stokes equations, including the Coriolis force. The 3D temperature field evolution was predicted by the model; salinity was kept constant at 0.05 psu. Realistic surface forcing fields (wind, atmospheric temperature and humidity, and solar radiation) were obtained by interpolating results of the COnsortium for Small-scale MOdeling (COSMO) atmospheric model of MeteoSwiss (Voudouri et al. 2017).

A description of the model configuration and validation was provided by Cimatoribus et al. (2018), based on Dorostkar et al. (2010) and Hill et al. (2012). A horizontal curvilinear grid with resolution of 173 m to 260 m was used and 35 depth layers in the vertical, with layer thickness ranging from 0.5 m at the surface to approximately 30 m in the deepest layer. The model was initialized from rest on 12 November 2013 at 12:00 (local time), with a horizontally uniform temperature profile as the initial condition, based on an observed profile collected on that date. The forward time integration used a time step of 20 s. Bottom friction was implemented as the frictional stress $\boldsymbol{\tau}_B = C_D \rho \|\mathbf{u}\| \mathbf{u}$, with $\rho$ the water density, $\mathbf{u}$ the velocity vector, and $\|\mathbf{u}\|$ its magnitude. The drag coefficient $C_D$ was set to 0.003 (Bouffard and Lemmin 2013). On the side boundaries, a free-slip condition was used. Vertical mixing was computed by the simple one-equation turbulence closure of Gaspar et al. (1990). Tests using a single column configuration and field observations at the SHL2 station (Fig. 1) showed that the parameter values from Gaspar et al. (1990) were appropriate when combined with an increased diffusivity under unstable stratification (0.02 $m^2\ s^{-1}$) to better model surface convection. Vertical stratification was found to be sensitive mainly to the background diffusivity, which was set to the molecular value based on similar single-column tests.

As demonstrated by Cimatoribus et al. (2018), the model realistically reproduced the stratification, mean flow, and internal seiche variability observed in the lake. As an example, in Fig. 2, temperature profiles observed on four different dates at station SHL2 (deepest point in the lake, red cross in Fig. 1a) are compared to those from the hydrodynamic model. The model reproduced the observed stratification throughout the year, without long-term drift after two years of simulation. A detailed validation of the model, based on both temperature and velocity measurements, was presented in the supplementary information of Cimatoribus et al. (2018). The model's main weak point is a tendency to underestimate velocity variability at periods shorter than approximately 10 h, due to the limited resolution of the model grid and of the forcing fields. Snapshots of the three components of velocity at each grid point were stored every 0.5 h from 12 December 2015 at 12:30 to the end of 2016. These velocity fields were used for the particle tracking simulations and are referred hereinafter as the "hydrodynamic simulation."

### Particle tracking

For particle tracking, the method described by Döös et al. (2013) was followed, as summarized in SI Appendix A. In this approach, particle trajectories, i.e., streamlines, were computed from the velocity field obtained with the hydrodynamic model, with linear interpolation of velocity in space (between model grid points) and in time (between flow snapshots). In

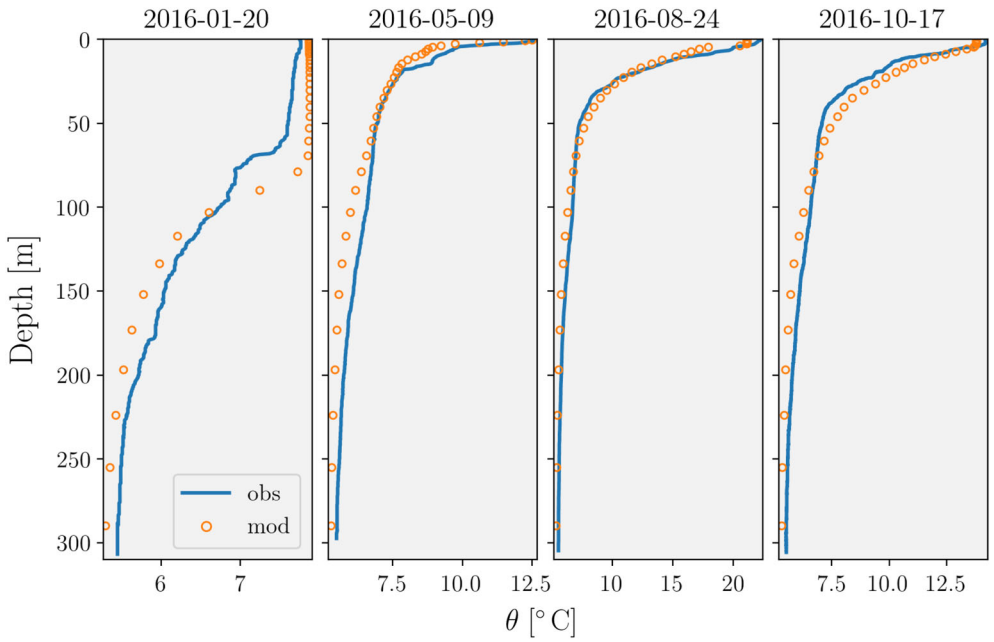


**Fig. 2.** Comparison between observed (blue lines) and modeled (orange circles) temperature stratification at SHL2 station (*see* Fig. 1), on 20 January, 05 May, 24 August, and 17 October 2016. Note that the horizontal axis is different in each panel.

**Table 1.** Summary of the particle tracking simulations performed. The simulation names are defined as follows: Y stands for yearlong, W for winter, and S for summer. *G* refers to the removal line near Geneva (western end of the lake), while *P* refers to the removal line at the entrance of the *Petit Lac*.

| Name | Start | End | Release | Removal |
|---|---|---|---|---|
| Y*G* | 12 Dec 2015 | 31 Dec 2016 | Continuous | Western end |
| W*G* | 01 Jan 2016 | 31 Mar 2016 | At start | Western end |
| S*G* | 15 Jun 2016 | 15 Sep 2016 | At start | Western end |
| Y*P* | 12 Dec 2015 | 31 Dec 2016 | Continuous | Confluence |
| W*P* | 01 Jan 2016 | 31 Mar 2016 | At start | Confluence |
| S*P* | 15 Jun 2016 | 15 Sep 2016 | At start | Confluence |

order to obtain convergence, the method used a time iteration, with 1000 intermediate time steps between two flow snapshots. No diffusion (e.g., by some random displacement) of the particles was allowed, as we focused on the deterministic advection by the flow resolved in the hydrodynamic model, and not on smaller-scale turbulent mixing. The algorithm was implemented by Cimatoribus (2018) using the Python language, translating and modifying the original Fortran code of Döös et al. (2013) to run on multiple processors, and accept the output format of MITgcm. Our code was tested by reproducing the analytical results discussed by Döös et al. (2013). Furthermore, it was confirmed that the results of the particle tracking were not sensitive to the choice of using flow field snapshots at 0.5 h intervals. This was also supported by the fact that the hydrodynamic model is known to have limited variability at this short time scale (Cimatoribus et al. 2018). An important feature of the tracking method employed in this study is that it conserves the volume, i.e., the no-flow side and bottom boundary conditions are respected by the computed trajectories, and no particles are lost from the basin.

Based on the velocity fields computed for 2016 by the hydrodynamic model, two series, *G* and *P*, consisting of three particle-tracking simulations each, are analyzed hereinafter (Table 1). In the analysis, a particle was no longer considered once it exited the simulation domain. The two series differed in the extent of the simulation domain. In series *G*, particles exited the domain if they reached the solid red line near the western end of the *Petit Lac* (near Geneva; Fig. 3a). Particles did not outflow through the gate, because the model cannot capture the dynamics therein. In series *P*, a particle trajectory was terminated if it reached the *Petit Lac* entrance at any depth (*see* solid red line at the confluence between the *Petit Lac* and *Grand Lac* in Fig. 3a). Two removal lines were chosen to investigate differences and similarities in transport between the two basins. In each of the two series, *G* and *P*, one simulation covered the entire period of the hydrodynamic simulation, from 12 December 2015 at 12:30 to the end of 2016 (simulations Y*G* and Y*P*, where Y stands for yearlong). The other two particle tracking simulations in each series explored the annual stratification cycle (Fig. 2). The first one covered the winter (W) period from 01 January to 31 March 2016 (simulations W*G* and W*P*), to study the weakly stratified dynamics, and the second one covered the summer (S) period from

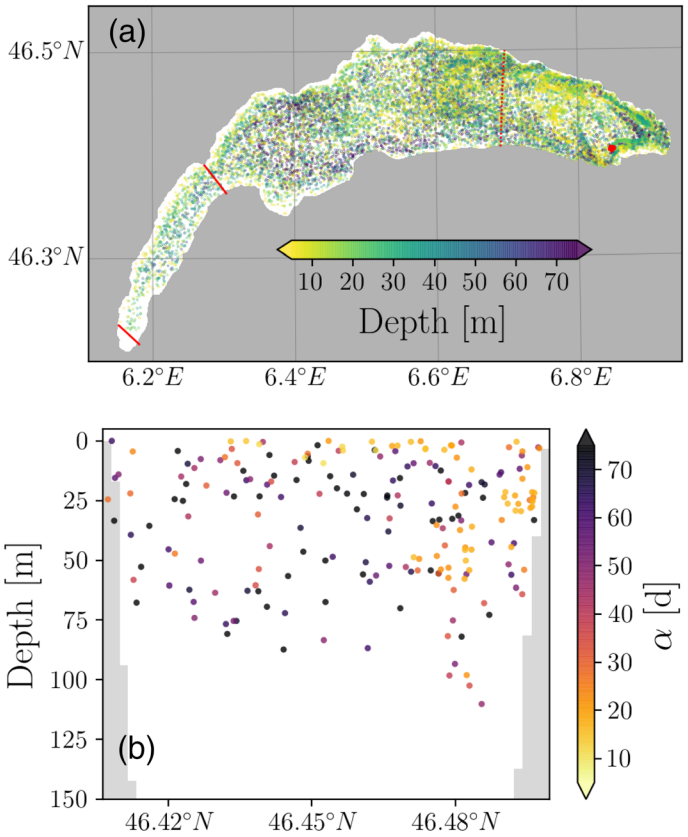


**Fig. 3.** (**a**) Similar to Fig. 1b, but showing particle position on 15 March 2016 at 00:30, and particles colored according to their depth. The particle removal lines, at the western end of the lake (*G*), as well as at the confluence between the two basins (*P*), are indicated with a red solid line. The release location is marked by a red dot at the eastern end of the lake. (**b**) Latitude–depth transect, along the dashed red line in (a). Particles within 1 km from the red dashed line of (a) are included, thus some particles appear to be below the lake bottom (gray shading), which refers to the center of the red transect. The age of the particles is given by the color bar in (b).

15 June to 15 September 2016, to analyze strongly stratified conditions (simulations S*G* and S*P*).

In all simulations, particles were released at the eastern end of the lake, within 1 km of the plunge point of the Rhône River (Fig. 3a) at nine different depths (5, 10, 15, 20, 25, 30, 50, 55, and 60 m). In the yearlong simulations, 33 particles were released every 4 h at each depth during the entire simulation, resulting in a total of approximately 700,000 particles. For each depth level, the initial conditions $\{\mathbf{x}_0\}$ were normally distributed horizontally, with a standard deviation of 100 m. Release points are marked by red dots that overlap at the scale used in Fig. 3a. An example of a computed trajectory from simulation S*G* is shown in Fig. 1a. The trajectory highlights the periods of smooth bathymetry-following motion, alternating with highly convoluted oscillations. At the end of the S*G* simulation, the particle was in the central region of the lake, even though it had previously almost reached the western end of the basin.

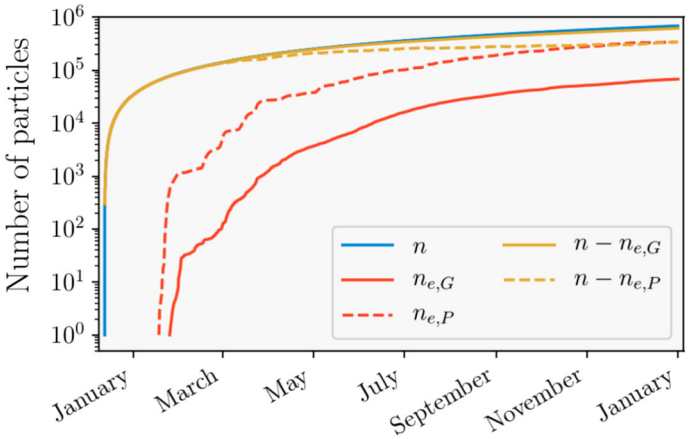


**Fig. 4.** Time series of the total number of particles released ($n$), and of the number of particles that exited the simulation domain ($n_e$), in the yearlong simulations. The horizontal axis marks every other month, from January 2016 to January 2017. The subscripts $G$ and $P$ of $n_e$ refer to the two simulation series (Table 1). The number of active particles $n - n_e$ is also shown.

For these yearlong simulations, Fig. 4 provides the time series of the total number of particles released ($n$, equal in the two series). It also indicates the number of particles that were removed from the simulation domain in the two series because they had reached the western end of the lake ($n_{e,\,G}$) or the *Petit Lac* ($n_{e,\,P}$). Furthermore, the number of active particles in the computation is shown ($n - n_{e,\,G}$ and $n - n_{e,\,P}$). A small fraction of particles exit the domain from the surface due to evaporation and neglecting motions of the free surface and are not considered here.

In each of the winter (W) and summer (S) simulations, 30,000 particles were released at each depth as in the yearlong simulations. Horizontally, the initial conditions were again normally distributed with a standard deviation of 100 m, centered outside the Rhône River mouth. All particles were released at the same time in a single batch at the beginning of each of these seasonal simulations. This allowed following the evolution of a particle cloud with better statistics than in the yearlong simulation.

### Residence time and dispersion

During the yearlong simulations, a small number of particles were continually released to study age and residence time. The age of the $i$-th particle, $\alpha_i$, is the time elapsed since its release; it is defined as long as a particle is inside the simulation domain. When the particle exits the domain, its age is the residence time, $\tau_i$, i.e., the time taken by a particle to reach a removal line from its release point.

To visualize how the residence time is related to the path that a particle follows in the lake (Fig. 1a), we proceeded as follows: the residence time $\tau_i$ was assigned to the points along the horizontal trajectory of the $i$-th particle. All trajectories in a given simulation were binned in space, using the

hydrodynamic model grid. For each bin, the mean residence time, $\overline{\tau}$, and its standard deviation, $\sigma_\tau$, were computed from the values $\tau_i$ found within that bin. For the winter simulations, all release depths were taken together (5–60 m), as trajectories tend to be more 3D in the presence of a weak stratification. For the summer simulations, two different depth ranges of release were considered separately (5–15 m and 20–30 m), as vertical motions were limited by the strong stratification (Fig. 2). For the same reason, no particle released below 30 m exited the domain in the summer simulation. These two ranges distinguished the upper layer and thermocline layers, respectively.

For the winter and summer simulations, the dispersion of particles within the domain can also be discussed in terms of the evolution of the variance of a cloud of particles, i.e., the squared dispersion radius (LaCasce 2008). This measures the relative dispersion with respect to the center of the particle patch. Both the horizontal and the vertical variances, indicated by $R_h^2(t)$ and $R_v^2(t)$, respectively, will be shown. The time dependence in the notation will be omitted hereinafter. The overestimation of the variances due to vertical shear was minimized by computing $R_h^2$ and $R_v^2$ in vertical bins of 0.25 m, following Steinbuck et al. (2011). Results were only mildly affected by this operation, mainly during the first month of the simulations. Variations at near-inertial frequencies were reduced the most after binning.

### Empirical orthogonal functions

Empirical Orthogonal Functions (EOFs) of the flow field (e.g., Hannachi et al. 2007) were computed. This technique identifies dominant variability patterns, or coherent structures, in a space- and time-varying field. Focusing on the first two patterns, which contribute the largest fraction of the total variance, we were able to determine the relationship between the flow field, the dispersion of particles, and the wind forcing.

To compute the EOF, the horizontal flux was considered, i.e., the vertically integrated horizontal velocity ($\mathbf{u}_h$):

$$\boldsymbol{\phi} = \int_{z_0}^{z_1} \mathbf{u}_h \, \mathrm{d}z,$$

where the integral is computed between the two (increasing) depths, $z_0$ and $z_1$. Flux $\boldsymbol{\phi}$ is a more relevant quantity than the vertically averaged velocity for understanding transport in the basin, and averaging $\mathbf{u}_h$ within depth ranges of more than a few meters tends to produce comparatively large velocities near-shore. As we were only interested in slowly evolving large-scale features, the $\boldsymbol{\phi}$ sampled at a time resolution of 2 h and at every other grid point on the hydrodynamic model was used. Areas in the vicinity of the Rhône River inflow and outflow were excluded from the analysis, to avoid including the discharge variability in the EOF.

Details on the EOF technique are given in SI, Appendix B. The EOF provides a set of modes, written as $\boldsymbol{\phi}^{(i)}$. This vector field with components $\phi_1^{(i)}$ and $\phi_2^{(i)}$ identifies a spatial pattern of the flux field. The time evolution of the flux field can be obtained from the EOF time coefficients, indicated as $c_1^{(i)}$ and $c_2^{(i)}$ for the two components, respectively. Each pattern $\boldsymbol{\phi}^{(i)}$, which evolves in time according to the time coefficients, captures a fraction of the total variance of the complete flux field $\boldsymbol{\phi}$. Only the first two EOF modes are presented, as they were the only ones that each captured more than 10% of the total variance.

The vector EOF modes $\boldsymbol{\phi}^{(i)}$ can be arbitrarily rotated (Legler 1983; von Storch and Zwiers 1999; Hannachi et al. 2007), which can greatly simplify their interpretation. This property was exploited, rotating the modes to concentrate the time-variability within one of the two components. The applied rotations rendered $c_1^{(i)}$ as large and $c_2^{(i)}$ as small as possible. After rotation, the time evolution of the vector pattern $\boldsymbol{\phi}^{(i)}$ is, to a good approximation, described by $c_1^{(i)}$ alone. The time coefficient $c_1^{(i)}$ determined changes mostly in the magnitude and in the positive or negative direction of the vectors of $\boldsymbol{\phi}^{(i)}$.

The coherent structures of the flow changed with time, in particular following the seasonal cycle, due to the different stratification and weather conditions. EOFs were thus computed separately for different periods during the year. Only the EOFs computed during summer are presented, using the hydrodynamic model results from 15 June to 15 September 2016, i.e., the same period as the summer particle tracking simulations (Table 1). During winter, no relation between EOF modes and particle dispersion was found. During summer, circulation is strongly baroclinic, due to the strengthening of the thermocline. For this reason, the EOF of the flux was computed in depth ranges similar to those used in the residence time analysis (see Residence time and dispersion in the Results section), i.e., from 5 to 20 m, and from 20 to 30 m.

## Results

From the single trajectory shown in Fig. 1a, some essential general characteristics of particle advection in Lake Geneva can already be inferred. The trajectory is highly convoluted, and extended unidirectional motion seldom occurs. The particle tends to move parallel to the isobaths, except at times when a change in the wind forcing causes an abrupt direction shift. When the particle enters the central region of the lake, it starts a series of circular motions, most likely related to inertial motions (Bauer et al. 1981).

Figure 1b provides further insight by showing the position of particles released at a depth of 20 m in simulation Y*G*, approximately 2 months after its start. Particles are colored according to their age. Older particles spread throughout the lake and were mixed rather uniformly from north to south, while a strong gradient persists in the east–west direction.

Younger particles cluster in well-defined patches, following to some extent the bathymetry, in particular along the northern shore. A predominantly anticlockwise circulation in the lake is consistent with the findings by Giovanoli (1990) and suggests a link to Kelvin waves (anticlockwise and shore intensified; Lemmin et al. 2005).

More details of the particle trajectories are seen in the animations presented in the SI. Two distinct patterns emerge: one of "rapid transit" trajectories focused in narrow bands mainly along the near-shore zone, and one of slower more spread out particle motion in the central region of the lake that often follow large-scale gyres that cover most of the lake basin. Both patterns last up to several days, and can be reactivated when favorable winds over the lake become stronger, as indicated by the arrows in the animations. Most often, "rapid transit" trajectories that start from the Rhône River delta are confined to the near-shore region along the northern shore of the *Grand Lac*, due to the Coriolis force. The particles can travel long distances, occasionally passing into the *Petit Lac* and reaching the removal line near Geneva within a few days. "Rapid transit" trajectories may at times also follow the southern near-shore region. This orientation is forced by a gyre established in front of the Rhône River delta. However, these particles typically cross over to the northern shore between two gyres in the central region of the *Grand Lac* and then may either follow the right gyre and return eastward toward the Rhône River mouth or the left gyre and move westward along the shore. The large gyres are highly variable in time. They eventually break down into smaller gyres, causing the particles to spread over large portions of the central lake region, finally filling most of this area (Fig. 1b). In the *Petit Lac*, particles frequently move toward the west along the northern shore almost to the end of the basin near the red line (Fig. 3a) and then back toward the east along the southern shore. A similar current pattern was reported by Betant and Perrenoud (1932). This pattern may in part be due to the shallow depth (average 5 m) in the region to the west of the red line.

The strong spatiotemporal inhomogeneity of the dispersion process is evident in Fig. 3 showing horizontal (panel a) and vertical (panel b) snapshots of particle positions from the yearlong simulation, about 3 months after the beginning of the simulation. Approximately 170,000 particles are active at this time. Only those released at a depth of 20 m are plotted. Figure 3a indicates that the particle distribution is still far from uniform, with generally higher concentrations near the boundaries, and denser clusters irregularly located in the *Grand Lac* (main basin). Furthermore, the depth of the particles (color coding in panel a) indicates that the particles were vertically displaced in a somewhat chaotic fashion. These large vertical displacements are typical of wintertime conditions, with weak stratification and stronger wind forcing than in summer. In summer, particles are trapped at their depth of release by the effect of stratification (*see* animations in the SI). Figure 3b offers an equally complex view along a vertical section. Particles are found at deeper depths along the northern shore, and younger particles (color coding) are downwelling therein. Finally, only older particles reached the interior.

Figure 4 shows the time series of the number of particles active in the yearlong simulations, Y*G* and Y*P*. It takes 1–2 months before the first particle exits the domain (red lines). It is somewhat unexpected that the time taken by the fastest particles to reach the western end of the lake (simulation Y*G*) is not much longer than the time needed to reach the *Petit Lac* (simulation Y*P*). The number of released particles ($n$) increases linearly in time, at the rate determined by the simulation setup. In contrast, the number of particles exiting the domain ($n_{e,\,G}$, $n_{e,\,P}$) increases irregularly, as a result of the intertwined effect of the variable wind-driven flow and the particle distribution in the domain. Toward the end of the yearlong simulations, less than 10% of all particles that were released reached the western end of the lake ($n_{e,\,G}$), and approximately 50% reached the *Petit Lac* ($n_{e,\,P}$). The system is, in both simulations, far from any statistical steady state (the logarithmic scale of Fig. 4 is in this sense misleading). Extrapolation has limited value, but assuming a constant $\mathrm{d}^2(n - n_{e,\,G})/\mathrm{d}t^2$, and estimating it from the yearlong simulation, one would expect a stationary state after $\mathcal{O}(10\ \mathrm{y})$. This is close to the mean flushing time (11 y, *see* Introduction), providing indirect support for the consistency of the presented numerical results.

**Residence time and dispersion**

Figure 5 presents histograms of residence times $\tau$ computed for all simulations. The black line, and the blue and green dots refer to the histograms of $\tau$ for the yearlong, winter, and summer simulations, respectively (upper panel series *G*, lower panel series *P*) without considering the different release depths of the particles. Residence times vary from several days to the full duration of the simulation. The $\tau$ distribution for the Y*G* simulation (panel a) peaks at 60–100 d, while for Y*P*, the peak is at shorter times (30–60 d), as expected. However, the right tails of these distributions are similar. This indicates that particles that remain trapped mainly recirculate in the *Grand Lac* basin.

More particles exited during summer than winter, as seen comparing the S*G* and W*G* simulations (Fig. 5a). The estimates of the $\tau$ distributions in these two shorter simulations are rather noisy. However, the distribution is overall flatter in summer than in winter. During winter, longer residence times are relatively more frequent, because particles, even if they rapidly fill the basin at all depths, tend to recirculate horizontally within gyres (*see* animations in the SI).

The three remaining histograms in each panel of Fig. 5 (light blue, orange, and yellow) distinguish between particles released in three different depth ranges in the yearlong simulations. Histograms are all very broad, and nearly all sampled residence times are possible, even if not equally probable,

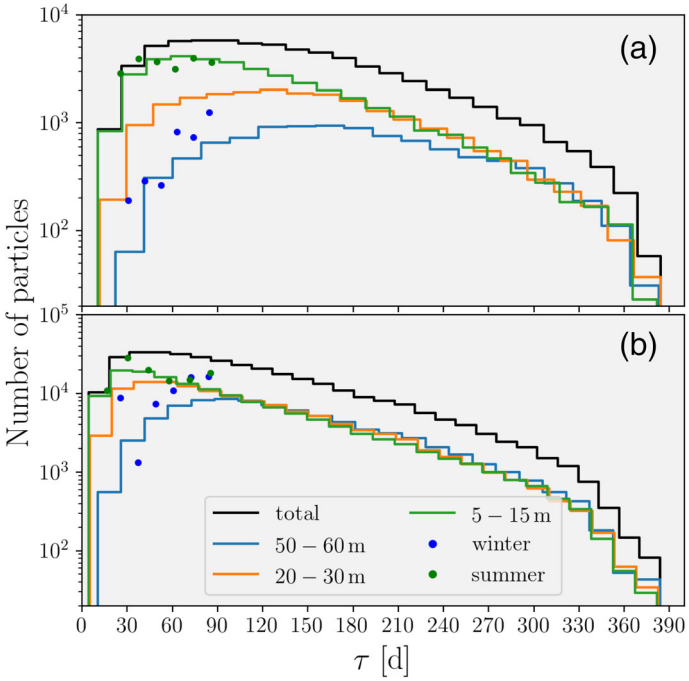


**Fig. 5.** Histograms of residence times. (**a**) (panel **b**) presents the results from the *G* series (*P* series) of simulations (Table 1). For the yearlong simulations, four histograms are given in each panel, distinguishing particles released in the following depth ranges: all depths, 50–60 m, 20–30 m, and 5–15 m (lines, legend in b). Histograms for the winter (W) and summer (S) simulations, each with a single-batch release, are also shown, without distinguishing between the different release depths (dots, *see* legend).

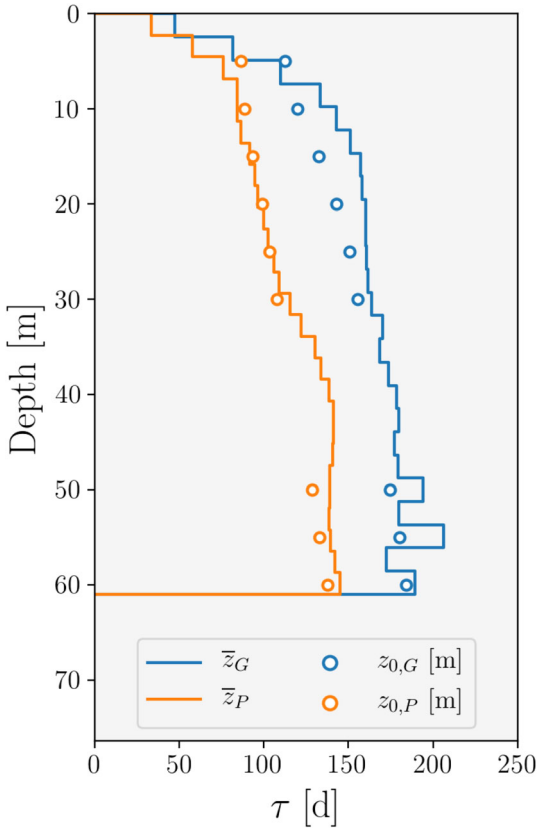


**Fig. 6.** Depth-dependence of the residence times from the yearlong simulations. The lines show the mean of these residence times as a function of the mean trajectory depth, computed in depth bins of approximately 2.5 m. The circles identify the mean residence time as a function of the initial release depth, $z_0$. Blue line and circles refer to simulation Y*G*, red ones to simulation Y*P* (Table 1).

regardless of the depth of release or simulation series. Fewer particles exit the simulation domains among those released at greater depths. Deeper particles move more in the vertical direction (Fig. 9), due to weaker stratification at depth, but only those that upwell at least to the depth of the *Petit Lac*, approximately 50 m, can eventually leave the domain. The particles released in the upper layer (5 – 15 m) tend to travel faster than those released at greater depths, because velocities decrease with depth. Furthermore, the histograms of shallower released particles have greater positive skewness. While the peak of the distribution (70 d in Y*G*, 30 d in Y*P*) is determined by particles reaching the removal lines approximately at the depth where they were released, particles downwelling into the deep lake can remain trapped therein for much longer times.

The depth dependence of the residence time is seen in more detail in Fig. 6, where $\tau$ from the Y*G* and Y*P* simulations is plotted as a function of depth. The mean residence time increases with both the depth of the initial release of particles ($z_0$, circles), and with the mean depth of the particle trajectory ($\overline{z}$, lines). The dependence of $\tau$ on $z_0$ and $\overline{z}$ is similar, but in Y*G*, $\tau$ increases faster with respect to $\overline{z}$ than to $z_0$, above 30 m. The shallow bathymetry of the *Petit Lac* hinders the westward transport of particles following deeper trajectories.

A more detailed analysis of dispersion in the winter and summer simulations allows understanding how seasonally varying conditions affect the residence times. Figure 7 assembles maps of the mean residence times along the particle trajectories using all trajectories from simulation W*P* (panel a) and S*P* (panels b and c). These maps provide an overview of how particle trajectories, following different pathways within the lake, tend, on average, to be associated with different residence times.

The mean residence time maps ($\overline{\tau}$, main panels) identify highly coherent "rapid transit pathways" in the lake. The rapid transit pathway mainly spans the southern half of the lake in W*P* (panel a), and in the S*P* upper layer (panel b). In the summer thermocline layer (panel c), the rapid transit pathway follows both the northern and southern shores in the eastern half of the *Grand Lac*. Further west, lower values of $\overline{\tau}$ concentrate in the northern half of the basin. From the maps of the standard deviation of the residence time, $\sigma_\tau$, (insets) one can infer that the standard deviation is approximately proportional to the mean. This implies a broader $\tau$ distribution

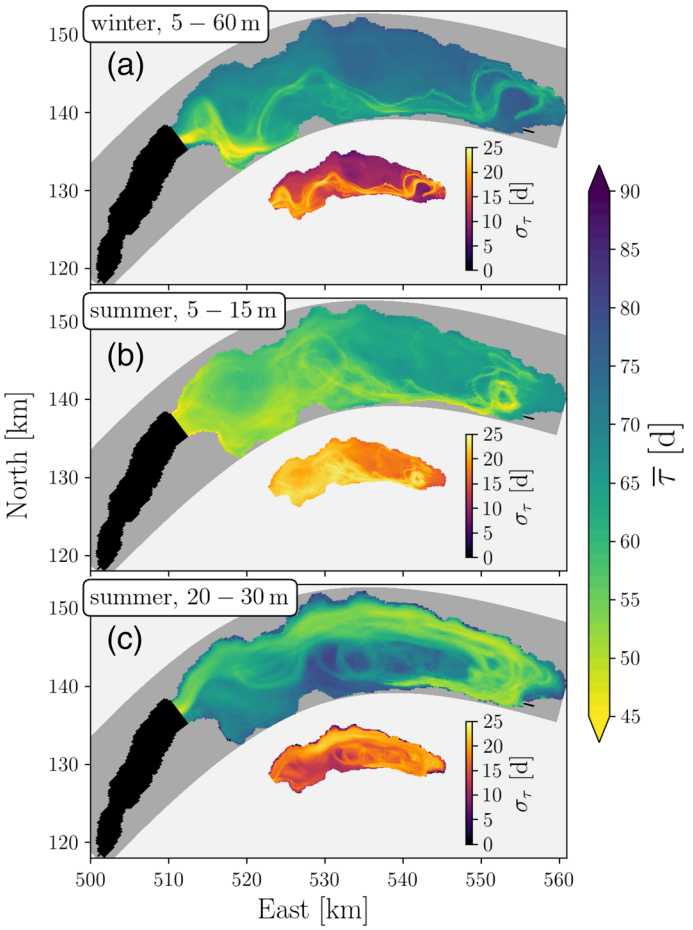


**Fig. 7.** Maps of the mean residence time $\overline{\tau}$ (main panels) and standard deviation $\sigma_\tau$ (insets) for simulations W*P* and S*P* (Table 1). From top to bottom, the three panels refer to: (**a**) simulation W*P*, using particles released in the 5–60 m depth range, (**b**) simulation S*P*, using particles released in the 5–15 m depth range (upper layer), (**c**) simulation S*P*, using particles released in the 20–30 m depth range (thermocline/upper hypolimnion). The Swiss Coordinate System is used for the plots.

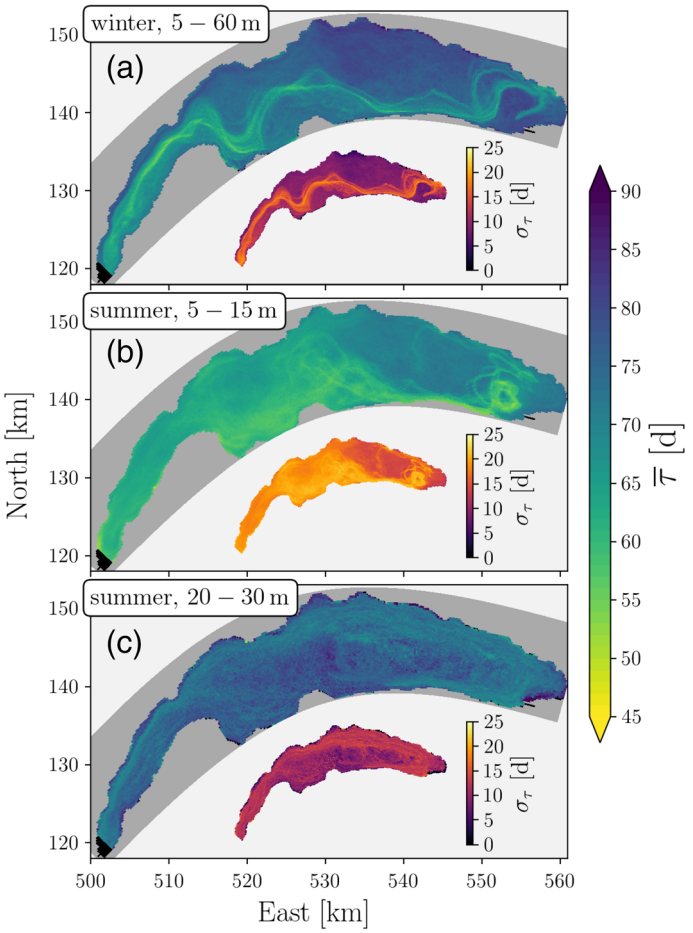


**Fig. 8.** Same as Fig. 7, for simulations W*G* and S*G* (Table 1).

in areas associated with rapid transit pathways, i.e., these rapid pathways are intermittent, and slower trajectories overlap with them at different times.

Figure 7 illustrates a preferential spreading route of the Rhône River interflow (panel c, the interflow spreads approximately at the thermocline depth) along the north shore and thus confirms the observations of Giovanoli (1990). However, the results indicate that, during summer, thermocline waters can also exit the Rhône River mouth area along the southern shore, but only up to the central region of the *Grand Lac*. Further west, this "southern pathway" effectively disappears, suggesting that intense stirring takes place there. Also note that the area centered at approximately 525 km East, 135 km North represents a "transport barrier," with a local maximum of $\overline{\tau}$. These findings are confirmed by the distributions of the particle trajectories (i.e., the spatial distribution of the number of trajectories), with more trajectories where the residence time is shorter (not shown).

During winter and in the summer upper layer (panels a and b), the results are very different, and particle trajectories are more uniformly distributed in the basin (not shown). Faster trajectories follow a more southern pathway, with evidence of vortical motion in the eastern part, and of enhanced dispersion in the western part of the *Grand Lac*. Given the uniform trajectory distribution, we suggest that the shorter $\overline{\tau}$ is associated in these cases with shorter paths, which particles follow during favorable wind conditions, further discussed below.

Figure 8 presents results similar to those discussed earlier, but computed from simulations W*G* and S*G*. As already discussed, fewer particles reach the western end of the lake and at least 10 more days are needed to reach Geneva, on average, after entering the *Petit Lac*. Despite these differences, the patterns are similar to those of Fig. 7 and extend in the *Petit Lac*, even if less well defined. One can thus conclude that the transport within the *Petit Lac* is rather uniform, and does not follow any preferential trajectory. Furthermore, particles first

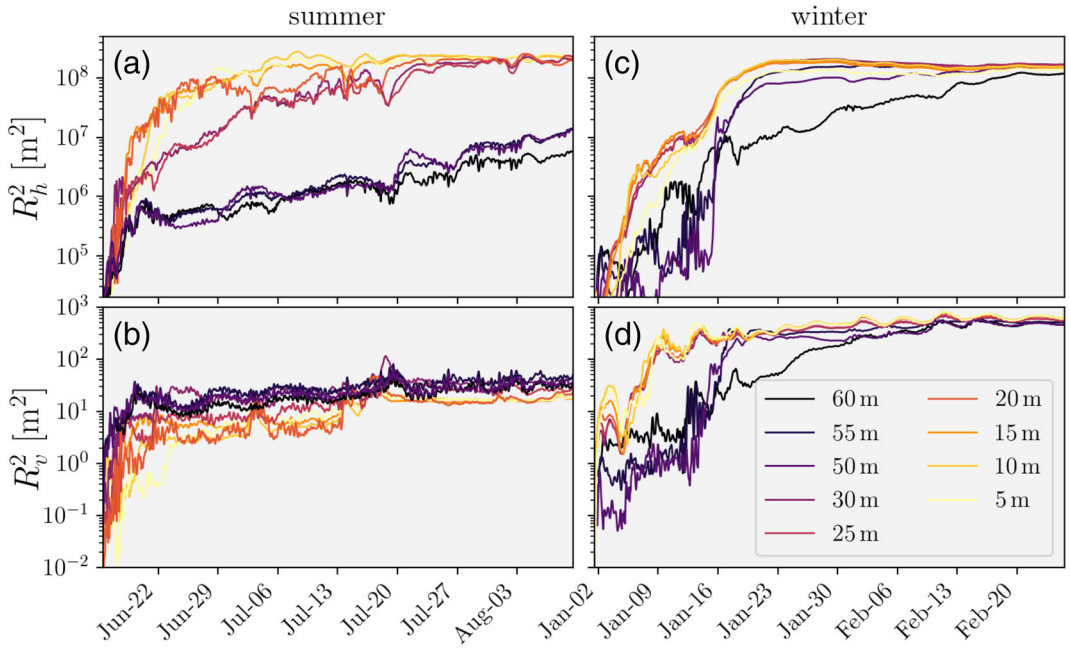


**Fig. 9.** Evolution of the horizontal and vertical squared dispersion radii in time. On the horizontal axis, dates are given as month-day of 2016. (**a**) and (**b**) refer to SG, (**c**) and (**d**) to WG. Only the first 55 d of the simulations are considered. In all panels, lines of different colors refer to different release depths of the particles (see legend in (d)). The upper (lower) panels show the time series of the horizontal (vertical) squared dispersion radius.

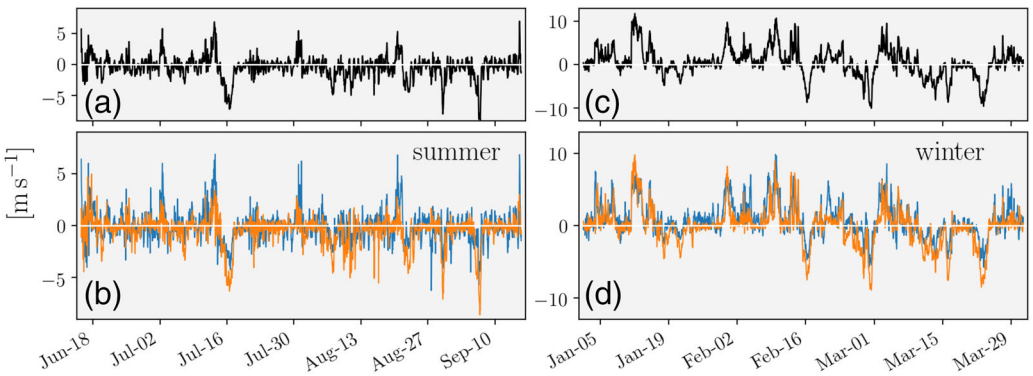


**Fig. 10.** Time series of the spatially averaged wind above the lake, during the summer (**a** and **b**) and winter (**c** and **d**) simulations. In (**b**) and (**d**), the two components of the wind are given: eastward in blue and northward in red. (**a**) and (**c**) provide the wind component along the southwest (negative, Bise) to northeast (positive, Vent) direction ($\widetilde{u}_A$, *see* text for details). The vertical scale is different between the left and right panels. On the horizontal axes, dates are given as month-day of 2016.

reaching the *Petit Lac* are also, on average, those that more rapidly reach the western end of the lake.

We suggested above that internal seiches may play a role in particle transport in Lake Geneva. To test this hypothesis, the time evolution of the squared dispersion radius was analyzed, i.e., the variances of the particle positions (Fig. 9). Results from S*G* and W*G* were considered, as the computation of the radius is only meaningful for a set of particles released together. Results for S*P* and W*P* were very similar and are thus not shown.

Dispersion is rather uniform in time, except for the deepest particles in winter (Fig. 10c,d), which respond to strong persistent winds blowing around mid-January. Some regular large amplitude wave motion is apparent during winter in the vertical dispersion (panel d), at periods of approximately 3 d (probably related to Kelvin mode 1). Closer to the surface, horizontal dispersion is initially faster in summer than in winter, but particles eventually fill the entire basin in a shorter time during winter (saturation level of $R_h^2$ in Fig. 9, *see* also animations in SI).

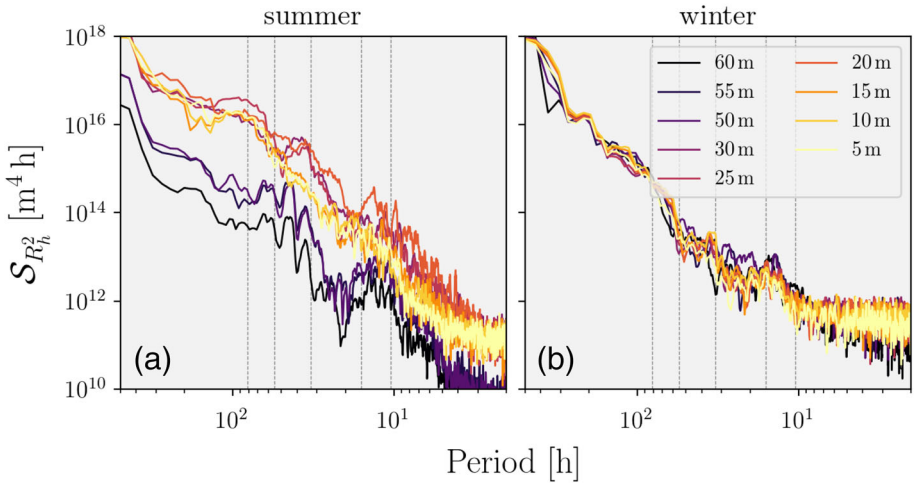


**Fig. 11.** Spectra of the $R_h^2$ time series of Fig. 9, for the SG (**a**) and WG (**b**) simulation. The colors of the lines refer to different depths (legend in **b**), as in Fig. 9. The vertical dashed lines identify the periods of some internal wave modes. From left to right, these are 81.5 h (Kelvin mode 1), 55.5 h (Kelvin mode 2), 33.3 h (Kelvin mode 3), 16.5 h (inertial/Coriolis), and 10.6 h (Poincaré mode 1).

During summer, the thermocline (approximately 20 m depth) separates particles spreading horizontally more rapidly above, from those below (panel a). On the other hand, deep particles spread faster in the vertical (panel b), as the weaker stratification in the hypolimnion allows more vertical motions than above the thermocline. During winter, with weak stratification in the whole water column, the dominant effect is related to the decay of surface forcing with depth. This results in an initially faster dispersion of the particles released closer to the surface, in both the horizontal and vertical directions (panels c and d). After approximately 2 months, the effect of the release depth is effectively lost, due to the large vertical displacements experienced by the particles.

The uniform increase of the dispersion radius suggests a negligible influence from internal wave motions. Further insight is gained by inspecting the spectra of the $R_h^2$ time series (Fig. 11). During winter, spectra at different depths are alike, with only a minor peak at near-inertial periods, and possibly at 33 h for shallower released particles. The effect of longer Kelvin modes (mode 1) is thus not detectable in $R_h^2$, but only in $R_v^2$, as noted above. During summer, spectral estimates vary more with depth, and deeper spectra (below approximately 15 m) have some small peaks. The spectral estimates are noisy, but some consistent results can be identified. Below 15 m, peaks at super-inertial periods and at the Kelvin mode 3 period (33 h) are present. Particles in the upper layers have enhanced variability near the Kelvin mode 1 period (81 h). A peak at periods of 50–40 h is also seen for the three deepest spectra, but cannot be attributed to any known internal wave mode.

Furthermore, spectra reveal that time variability at periods shorter than approximately 100 h is more pronounced during summer than winter, with the exception of the three deepest curves. This is probably linked to the kinetic energy trapping effect of the summer thermocline. Overall, the analysis suggests that the effect of internal seiches is small, even if it can be identified. Slower motions, related with the mean response to wind forcing, are thus more likely driving dispersion in Lake Geneva.

### Linking dispersion to flow and wind forcing

Figures 12 and 13 present the EOF of the flux computed in the depth ranges from 5 to 20 m and from 20 to 30 m, respectively, based on the summertime simulation SG. The fraction of the variance represented by each mode in the two depth ranges is given in Table 2. The same analysis was carried out for the winter case, but it did not provide any additional insight concerning particle dispersion and is thus not shown. This seems to be due to the more rapid spreading of the particles throughout the basin during the winter (*see* Residence time and dispersion in the Results section).

In Fig. 12, the first EOF mode in the summertime upper layer mainly consists of a flow from east to west, and from the southern to the northern shore in the central part of the basin. In the second mode, a two-gyre pattern, of unequal intensity, is apparent, anticlockwise in the eastern part of the lake and clockwise in the west. The western gyre partially enters the *Petit Lac*, even if recirculation within the *Grand Lac* is present. Some correlation could be established between $\boldsymbol{\phi}^{(1)}$ in Fig. 12 and the "rapid transit" pathway in the central panel of Figs. 7 and 8, mainly in the eastern part of the lake. Such a link was not evident for the second mode. In terms of time coefficients (Fig. 12d), the main component of the two modes ($c_1^{(i=1,2)}$) is excited approximately at the same time by the wind (Fig. 10), but the peaks are out of phase. The spectral distributions of $c_1^{(i=1,2)}$ are given in Fig. 12c. The spectra of $c_1^{(i)}$ for the two modes are similar, with broad peaks at the periods of Kelvin modes 1 and 2, and at near-inertial periods. The peaks are slightly more pronounced for $c_1^{(1)}$.

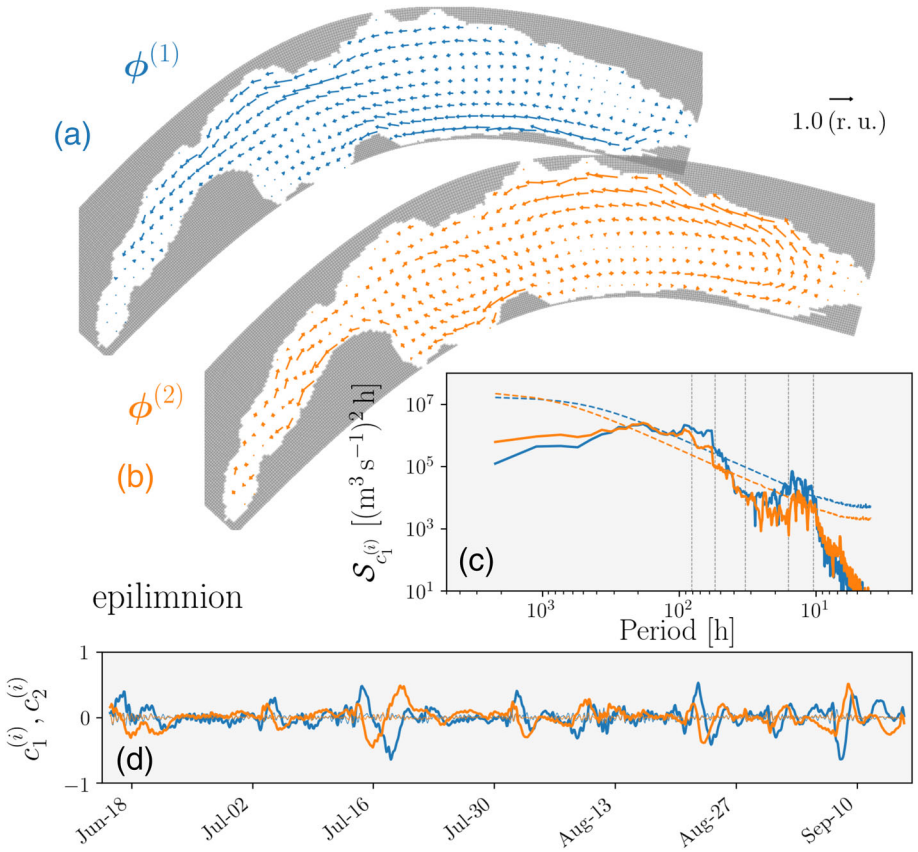


**Fig. 12.** First two EOF modes of the flux $\boldsymbol{\phi}$, in the depth range between 5 and 20 m for the summer simulation SG. The spatial structure of the modes is shown in the two maps, in (**a**) and (**b**), respectively (mode $i = 1$ in blue, mode $i = 2$ in orange). The time coefficients of the two modes (units of $10^3$ m$^3$ s$^{-1}$) are reported in (**d**), with colors corresponding to those of the maps. Dates on the horizontal axis are given as month-day of 2016. The two components of the coefficients, $c_1^{(i)}$ and $c_2^{(i)}$, are given by the thick and thin lines, respectively. Spectra of the $c_1^{(i)}$ time coefficients are plotted in (**c**) (solid lines), with 99% significance levels, based on an autoregressive lag 1 model (dashed lines using the corresponding colors). The periods of some internal wave modes are marked by vertical dashed lines. From left to right, the periods are 81.5 h (Kelvin mode 1), 55.5 h (Kelvin mode 2), 33.3 h (Kelvin mode 3), 16.5 h (inertial/Coriolis), and 10.6 h (Poincaré mode 1).

The results suggest a link between the "rapid transit" path and $\boldsymbol{\phi}^{(1)}$ for the summertime upper layer. This can be tested by considering cross correlations between EOF modes, wind forcing and dispersion. The time series of the two horizontal wind components (blue and orange in Fig. 10b,d) confirmed that the wind is mostly aligned along the southwest to northeast direction. As a representative "wind index," it was thus used the component of the wind along this direction, $\widetilde{u}_A$, effectively an approximation of the first wind EOF (Fig. 10a,c). It is positive or negative, respectively, when the Vent or Bise is blowing, and its magnitude is close to the (mean) wind speed. As a measure of dispersion, the time increments of $R_h^2$ were considered, written as $\Delta R_h^2$, and averaged in the relevant depth range. Increments were used, rather than the time series itself, to reduce nonstationarity (e.g., Percival and Walden 1993).

The lagged cross correlation was computed between the EOF coefficients $c_1^{(i)}$, and either the squared radius increments ($\gamma\left[c_1^{(i)}, \Delta R_h^2\right]$) or the wind index ($\gamma\left[\widetilde{u}_A, c_1^{(i)}\right]$). Squared radii were obtained from the SG and WG simulations. The results for the upper layer during summer are given in Fig. 14a,b. The cross correlation between $c_1^{(i)}$ and $\Delta R_h^2$ (panel a) is never larger than 0.3 in absolute value. For the first EOF mode, $\gamma\left[c_1^{(1)}, \Delta R_h^2\right]$ peaks clearly beyond the 99% significance level at lag 0 h (positive peak), 46 h (negative peak), and 80 h (positive peak). For the second EOF mode, the only peak that can be distinguished from the significance level is at −18 h (negative peak). The cross correlation between $c_1^{(i)}$ and the wind reaches values larger than 0.6 in absolute value. EOF mode 1 is excited by the wind with a lag of 20 h. The peak of $\gamma\left[\widetilde{u}_A, c_1^{(1)}\right]$ is positive, which means that $c_1^{(1)}$ has the same sign as the wind that excited it. For example, this lagged response can be identified in the time series of Figs. 10 ($\widetilde{u}_A$) and 12 ($c_1^{(1)}$) between 10 and 16 July 2016. EOF mode 2 is excited at a lag of approximately 32 h, with a sign opposite to the wind. A smaller positive

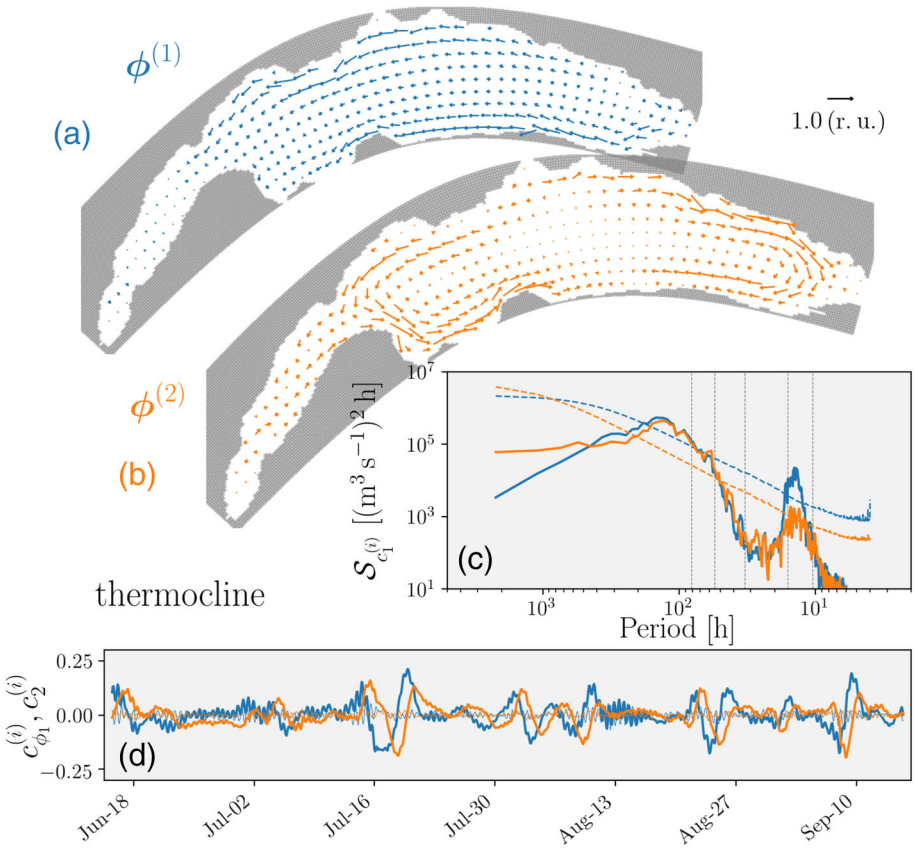


**Fig. 13.** Same as Fig. 12, for the flux $\boldsymbol{\phi}$ in the depth range between 20 and 30 m.

**Table 2.** For the summer simulation SG: fraction of the total variance of the flux field captured by the first two EOF modes, for the two depth ranges considered.

| Depth range | $\sigma^{2,(1)}/\sigma^2_{tot}$ | $\sigma^{2,(2)}/\sigma^2_{tot}$ |
|---|---|---|
| 5 – 20 m | 0.27 | 0.16 |
| 20 – 30 m | 0.21 | 0.13 |

peak is seen at 9 h; despite its uncertain statistical significance, a careful comparison of the time series confirms this more rapid, but weaker response of $c_1^{(2)}$.

The sequence of events in the summer upper layer can be summarized as follows. The EOF mode 2 is weakly excited by the wind after less than 12 h, $\boldsymbol{\phi}^{(1)}$ peaks after less than 24 h, and finally $\boldsymbol{\phi}^{(2)}$ gains more energy, with a reversed pattern with respect to the initial response. The sequence is similar for the two wind directions, with flow patterns having reversed signs. In terms of dispersion, the link with the EOF modes is weaker. However, cross correlations indicate that a positive $c_1^{(1)}$ tends to enhance dispersion at first, and to limit it after approximately 48 h. This means that the Vent (positive $\widetilde{u}_A$) tends to enhance dispersion after approximately 12 h from its onset, and reduces it later on. The opposite is true for the Bise (negative $\widetilde{u}_A$), which reduces dispersion at first, and enhances it afterward. Considering the $\boldsymbol{\phi}^{(1)}$ pattern in Fig. 12, it is obvious that a positive $c_1^{(1)}$ determines westward advection in the upper layer that enhances the dispersion of the particle patch originating from the Rhône River mouth area. For EOF mode 2, the link to dispersion was less evident. The negative lag of the peak in $\gamma\left[c_1^{(2)}, \Delta R_h^2\right]$, combined with the positive one of $\gamma\left[\widetilde{u}_A, c_1^{(2)}\right]$, implies that dispersion is enhanced before $c_1^{(2)}$ reaches a minimum, approximately 12 h after the onset of a Vent wind. This is probably a spurious correlation: 12 h after the onset of Vent, $c_1^{(1)}$ is at its maximum and enhances dispersion, while $c_1^{(2)}$ is close to zero; little flux is thus actually captured by $\boldsymbol{\phi}^{(2)}$.

A similar analysis was carried out in the thermocline layer, 20–30 m depth, again for the summer simulation. In this case, the first EOF mode (Fig. 13) captures part of the near-inertial response to wind forcing, as demonstrated by spectral analysis, and the lagged correlation $\gamma\left[\widetilde{u}_A, c_1^{(1)}\right]$ (Fig. 14d), which peaks first at near-inertial periods. However, a longer term response is included in $\boldsymbol{\phi}^{(1)}$, responding to the wind

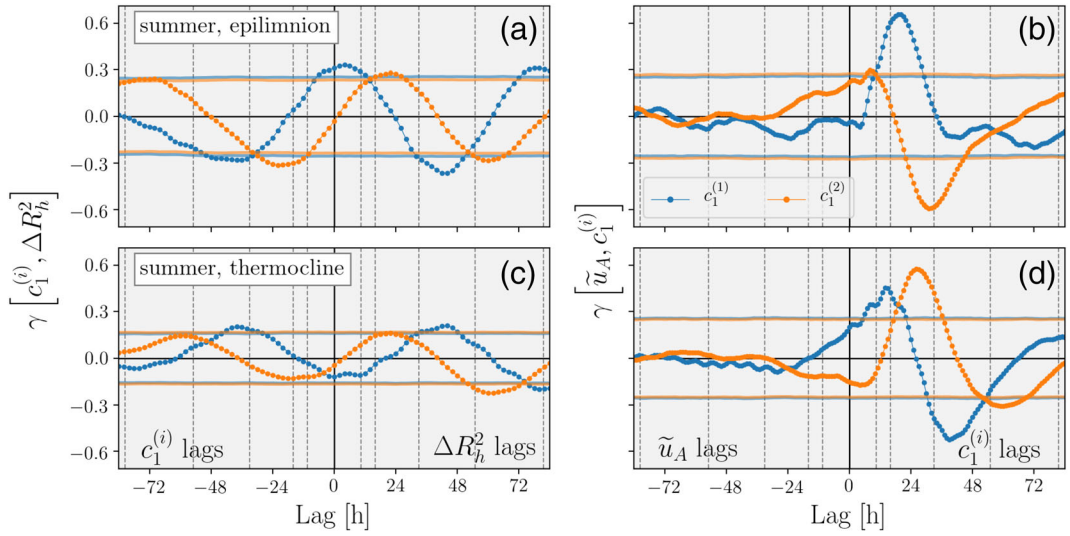


**Fig. 14.** (**a**) and (**c**) Cross correlation of mode coefficients $c_1^{(i)}$ with squared radius time increments $\Delta R_h^2$. (**b**) and (**d**) Cross correlation of the "wind index" $\widetilde{u}_A$ with $c_1^{(i)}$. The upper (lower) panels refer to the 5–15 m (20–30 m) layer, for the summer simulation SG. The line-connected dots are the cross correlation value, while the thick lines are bootstrapping-derived 99% significance levels (Ebisuzaki 1997). Blue refers to EOF mode $i = 1$ and orange to EOF mode $i = 2$. The periods of internal wave modes (10.6, 16.5, 33.3, 55.5, and 81.5 h, positive and negative) are marked by vertical dashed lines.

(with opposite sign) on time scales between 36 and 48 h. The EOF pattern $\boldsymbol{\phi}^{(1)}$ is composed of two near-shore westward parallel currents, which most likely correspond to a displacement of the thermocline along the major axis of the lake. Despite the clear spectral signature of near-inertial waves, the Poincaré mode computed by Lemmin et al. (2005) is not evident in Fig. 13. The difficulty in recognizing theoretically predicted physical modes in EOFs is a well-known and unavoidable limitation of the decomposition method. In the present case, longer time-scale motions dominated in the spectrum, i.e., they induced larger variations that dominate the EOF pattern of $\boldsymbol{\phi}^{(1)}$.

The EOF mode 2 pattern in this deeper layer is a double gyre located mainly in the *Grand Lac*, somewhat similar to the one in the upper layer, but with reversed direction. The cross correlation $\gamma\left[\widetilde{u}_A, c_1^{(2)}\right]$ indicates that excitation by the wind becomes evident after a lag of approximately 24 h, and with equal sign. Correlations between EOF modes and dispersion are, in this deep layer, even smaller than in the upper layer. Some enhancement of dispersion by a negative $c_1^{(2)}$ is captured, with a lag of approximately 60 h (Fig. 14c). This implies a larger $\Delta R_h^2$ approximately 72 h after a Bise wind, which in this case could also be linked to the westward advection (negative $c_1^{(2)}$) in the eastern part of the *Grand Lac*. Some enhancement of dispersion by positive $c_1^{(1)}$ with a lag of approximately 48 h is seen. Despite the low correlations, a correspondence is evident between the EOF mode patterns shown in Fig. 13, particularly $\boldsymbol{\phi}^{(2)}$, and the residence time maps in Figs. 7c and 8c, especially in the eastern part of the lake.

**Age distribution**

Using the yearlong simulation (YG), the age distribution in the lake was investigated. Figure 15 summarizes the evolution of the Probability Density Function (PDF) of age ($\alpha$) and residence time ($\tau$), obtained from the YG simulation. The PDF was computed from the histogram of the data; the number of bins was based on Doane's formula (Doane 1976), but the results were not sensitive to this choice. The two distributions broaden as the simulation progresses and new particles are continuously released. The two distributions, however, do not evolve in the same way, as is more clearly seen from their ratio (upper panels), often referred to as the age function (e.g., Benettin et al. 2013). At earlier times (Fig. 15a,b), the domain was not yet filled by the particles released in the east (Fig. 1b), and the right tail of the residence time PDF is fatter than that of the age ($\tau/\alpha > 1$). Older particles preferentially reach the removal line, simply because they had more time to actually arrive there. Later on (panels c and d), however, the ratio between $\tau$ and $\alpha$ in the right tail becomes smaller than unity. This means that older particles were more likely than younger ones to remain in the basin at this time, as also was the case when summer stratification was eroded during fall (panels e and f). We suggest that this partial "trapping" effect is persistent rather than seasonal. However, it can be seen in Fig. 15 that the values at which $\tau/\alpha < 1$ increase with time, meaning that the trapping is effective only for the oldest particles still in the domain.

To understand how this trapping is related to the spatial distribution of particles, reference should be made to Fig. 16, where two maps of the mean age ($\overline{\alpha}$) of particles at the end of

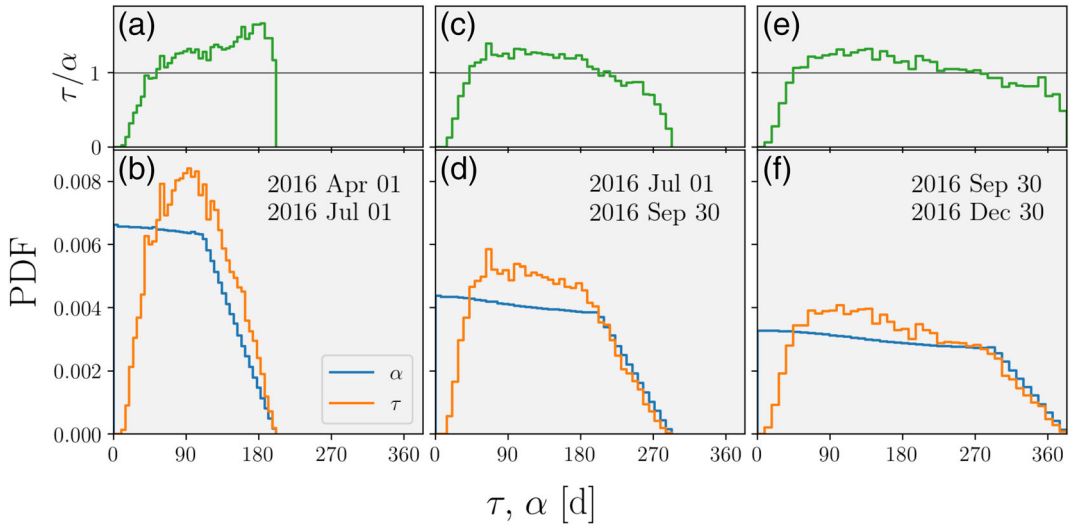


**Fig. 15.** The lower panels (**b**, **d**, **f**) show the PDF of age $\alpha$ (blue) and residence time $\tau$ (orange). The upper panels (**a**, **c**, **e**) show the ratio between the PDFs of these two quantities. From left to right, the panels refer to results computed considering different time intervals in the YG simulation: 1 April to 1 July, 1 July to 30 September, and 30 September to 30 December 2016. For age (residence time), particles active (particles reaching the western end of the domain) during the respective time intervals were considered.

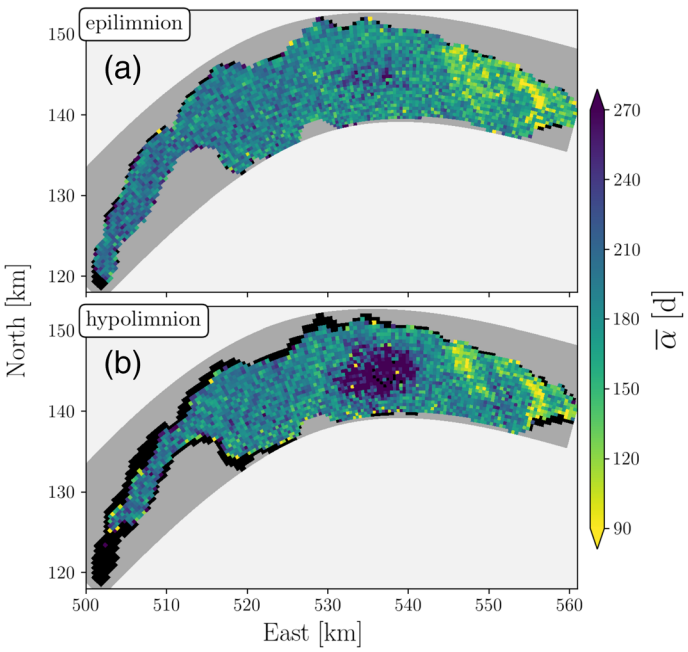


**Fig. 16.** Maps of mean age at the end of the yearlong simulation (YG). The mean is computed binning particles, based on their end position, in two depth ranges and in horizontal bins defined by the hydrodynamic model grid (at halved resolution). (**a**) refers to the 5–15 m depth range, and (**b**) to the 50–60 m depth range. The black areas have no particles in the considered depth range.

the YG simulation are shown. Panel a (panel b) displays particles that are at a depth between 5 and 15 m (50 and 60 m) at the end of the simulation. The estimates of $\overline{\alpha}$ are noisier than those of $\overline{\tau}$ (Fig. 8) because the spatial binning used to compute $\overline{\alpha}$ only considered the final position of each active particle, and not the entire trajectory (thus, larger spatial bins were used). In the upper layer (Fig. 16a), the age decreased from west to east, approaching the particle release area. On top of this small background trend, patches of young particles were present in the eastern part of the lake, closer to the northern shore. This is a further demonstration of the intermittent nature of particle advection, and it is consistent with the above shown preference for westward advection along the northern shore. In the central region of the *Grand Lac*, an area with a slightly higher mean age was seen. Deeper in the lake (Fig. 16b), older particles were found in the center of the *Grand Lac*, and became the dominant feature on the map. Figure 16 strongly suggests that particles can remain trapped in the central deeper part of the *Grand Lac*, even if they continue to move, recirculating in this area. Furthermore, fewer particles were overall present in this region (not shown), indicating that transport from and toward this region was hindered. The persistent vortical flow in this part of the lake (*see* animations in SI) seems to act as an effective barrier to transport. The existence of such barriers is not unusual in lakes or other geophysical flows (e.g., Chen et al. 2002).

## Discussion and conclusions

Our results shed new light on transport processes in Lake Geneva, in particular documenting the large spatiotemporal variability of transport. Even when relatively simple spatial particle patterns were observed, these may in fact result from the accumulation of particles having different ages (Fig. 3b). The existence of relatively well-defined rapid transit paths and of trapping regions provided further confirmation of the inhomogeneity of transport in the lake. For these reasons, care

should be taken when using spatial distributions of sediments or stable isotopes in the lake to infer more general transport dynamics, e.g., relevant for reactive species or biological activity. Sediments and stable isotopes carry no information on residence time in the lake, and thus could hide an important part of the transport variability. This has practical implications, as the rapid transport of highly localized patches of, e.g., a pollutant could have an entirely different ecological impact than a more uniform dispersion. The same holds true if a pollutant remains trapped for a long time in the central, deep region of the lake.

The relationship of particle dispersion with wind forcing and lake currents was described, but the strong variability of forcing and currents prevents a complete explanation in terms of only a few flow EOF modes. On the other hand, changes in stratification strongly affected the dispersion dynamics, thus enabling the prediction of the average dispersion behavior for different seasons. In particular, strong summer stratification limits vertical displacements, shielding the deep lake from the surface forcing, enhancing at the same time variability of dispersion in the upper layer (Figs. 9 and 11). For example, in order to exit the lake, a water parcel must upwell to the surface layer. An increase in stratification due to warmer summer or milder winter conditions may thus lead to a further slowdown of water renewal at depth.

Although not dominant, the importance of the lake's internal wave modes for transport could be identified (mainly from Fig. 11). Stocker and Imberger (2003) demonstrated that dispersion by internal seiches is mainly a reversible process, as confirmed here by the fact that the near-inertial peak of the squared radius spectra was reduced when applying the method described in Steinbuck et al. (2011) (*see* Residence time and dispersion in the Methods section). The time evolution of the squared radius suggests that Kelvin waves play a non-negligible role for particle dispersion, even though Cimatoribus et al. (2018) found that they are not important in the mean energy balance of the near-shore region. The shore-hugging nature of the EOF mode patterns (similar to the "rapid transit" paths in Fig. 8) and the spectral distribution of the EOF time coefficients further support the importance of Kelvin modes for transport. It is in the 20–30 m depth range, where Kelvin waves are expected to have their maximum amplitude, that their spectral signature was most clearly identified in the particle dispersion (Fig. 11a). This agrees with the results of Umlauf and Lemmin (2005), although the importance of Kelvin waves for the exchange of deep water between the *Grand Lac* and the *Petit Lac* was not discussed in detail here.

The simulations presented cannot provide complete answers about the water renewal mechanism in Lake Geneva, in particular concerning the trapping of particles (i.e., of water) at depth in the central region of the lake (*see* Age distribution in the Results section). In this context, one must also consider the occurrence of infrequent winter mixing events (full-depth overturning), due to shear (wind forcing) and/or convection (cooling). As noted in the Introduction, the near-shore variability of the Rhône River inflow, which can lead to gravity currents reaching great depths, is an additional uncertainty element that deserves future attention. Although these processes were not examined in detail, the strong wind event on 15 January 2016, which caused a sudden increase in $R_v^2$ of deeper particles (Fig. 9, winter), confirmed the importance of wintertime storms for dispersion of particles at greater depth.

Furthermore, mixing at scales unresolved by the hydrodynamic grid used in this study, $\mathcal{O}(200\ \mathrm{m})$ horizontally, could enhance dispersion in both horizontal and vertical directions. It is unlikely that such mixing can substantially reduce the spatial inhomogeneity of transport on time scales of days or weeks, but may reduce the trapping of water, particles or compounds over longer periods. However, shear-induced mixing is expected to be small at depth, where particle trapping was observed. The extension of the simulations to longer time scales, e.g., several years, is also of clear interest in this context.

Halder et al. (2013) suggested that water from the Rhône River can reach the *Petit Lac* in about 5 months (or less). Our results indicated that shorter residence times (in the *Grand Lac*) are actually more frequent, not only near the surface, but also within the thermocline layer where the interflow is located (Fig. 5b, red line).

From a water management point of view, this study made evident two important elements. First, we demonstrated that transport in Lake Geneva is far from being a homogeneous smooth process. Therefore, contaminants/pollutants from a point source will most likely spread in an inhomogeneous and intermittent manner, at least before small-scale turbulent diffusion (neglected in our particle tracking simulations) smooths the horizontal gradients (days to weeks). This, in turn, hinders predicting with precision how a pollutant patch will spread, and thus measurements taken at a single station will not provide reliable information about the mean concentration of a recently released tracer. Second, our results visually captured the existence of preferred transport pathways in Lake Geneva, mainly located along the northern shore. Pollutants or other tracers from the Rhône River will rapidly first reach and then leave these areas of enhanced water renewal. The deep central part of the *Grand Lac* and, to a lesser extent, its southwestern portion are, on the other hand, relatively isolated from the rest of the lake. Therefore, mixing with the Rhône River waters and with other runoff water is slower there. As a result, these areas risk developing into potential hot spots for the accumulation of persistent pollutants and for deoxygenation.

This study provided the first detailed numerical characterization of dispersion dynamics in Lake Geneva, focusing on the east-to-west transport and on intra-annual time scales. We encourage the experimental verification of the predictions discussed in this paper. Specifically, the field verification of the spatial links between age and residence time distributions

would provide an important validation of this study, and in general contribute to the development of effective lake water management concepts. For this purpose, the analysis of diluted tracers, released upstream in the Rhône River, would probably offer the most interesting insights, but would imply at the same time an important observational effort (frequent monitoring at several locations in the lake). The use of drogues tracked by GPS would permit a simpler alternative to perform more localized studies. We hope that this work will motivate further attention on these aspects, and contribute to a better understanding of transport processes in Lake Geneva and similar water basins.

## References


Arakawa, A., and V. R. Lamb. 1977. Computational design of the basic dynamical processes of the UCLA general circulation model. In General circulation models of the atmosphere, ed. by J. Chang, **17**:173–265. Elsevier. doi:10.1016/B978-0-12-460817-7.50009-4

Bauer, S. W., W. H. Graf, C. H. Mortimer, and C. Perrinjaquet. 1981. Inertial motion in Lake Geneva (le Léman). Arch. Meteorol., Geophys. Bioklimatol., Ser. A **30**: 289–312. doi:10.1007/BF02257850

Bäuerle, E. 1985. Internal free oscillations in the Lake of Geneva. Ann. Geophys. **3**: 199–206.

Benettin, P., A. Rinaldo, and G. Botter. 2013. Kinematics of age mixing in advection-dispersion models. Water Resour. Res. **49**: 8539–8551. doi:10.1002/2013WR014708

Betant, A., and G. Perrenoud. 1932. Etudes sur la partie occidentale du lac de Genève. Albert Kundig: Geneva, Switzerland.

Bonvin, F., R. Rutler, N. Chèvre, J. Halder, and T. Kohn. 2011. Spatial and temporal presence of a wastewater-derived micropollutant plume in Lake Geneva. Environ. Sci. Technol. **45**: 4702–4709. doi:10.1021/es2003588

Bouffard, D., and U. Lemmin. 2013. Kelvin waves in Lake Geneva. J. Great Lakes Res. **39**: 637–645. doi:10.1016/j.jglr.2013.09.005

Chen, C., J. Zhu, K. Kang, H. Liu, E. Ralph, S. A. Green, and J. W. Budd. 2002. Cross-frontal transport along the Keweenaw coast in Lake Superior: A Lagrangian model study. Dynam. Atmos. Oceans **36**: 83–102. doi:10.1016/S0377-0265(02)00026-X

Cimatoribus, A. A. 2018. *C-tracker*. C-tracker can be downloaded from zenodo.org. doi:10.5281/zenodo.1034118

Cimatoribus, A. A., U. Lemmin, D. Bouffard, and D. A. Barry. 2018. Nonlinear dynamics of the near-shore boundary layer of a large lake (Lake Geneva). J. Geophys. Res.: Oceans **123**: 1016–1031. doi:10.1002/2017JC013531

Conseil scientifique de la commission internationale pour la protection des eaux du Léman contre la pollution. 2017. Rapports sur les études et recherches entreprises dans le bassin lémanique. Campagne 2016. [accessed 2018 May 25]. CIPEL. Available from http://www.cipel.org/publications/rapports-scientifiques/rapport-2017-campagne-2016/.

Doane, D. P. 1976. Aesthetic frequency classifications. Am. Stat. **30**: 181–183. doi:10.1080/00031305.1976.10479172

Dominik, J., D. Burrus, and J. P. Vernet. 1983. A preliminary investigation of the Rhône River plume in eastern Lake Geneva. J. Sediment. Petrol. **53**: 159–163. doi:10.1306/212F817A-2B24-11D7-8648000102C1865D.

Döös, K., J. Kjellsson and B. Jönsson. 2013. TRACMASS-A Lagrangian trajectory model. In Preventive methods for coastal protection, ed. by T. Soomere and E. Quak, 225–249. Springer International Publishing.

Dorostkar, A., L. Boegman, P. J. Diamessis and A. Pollard. 2010. Sensitivity of MITgcm to different model parameters in application to Cayuga Lake. In Environmental Hydraulics, Two Volume Set: Proceedings of the 6th International Symposium on Environmental Hydraulics, Athens, Greece, 23–25 June 2010, 373.

Ebisuzaki, W. 1997. A method to estimate the statistical significance of a correlation when the data are serially correlated. J. Climate **10**: 2147–2153. doi:10.1175/1520-0442(1997)010<2147:AMTETS>2.0.CO;2

Gaspar, P., Y. Grégoris, and J.-M. Lefevre. 1990. A simple eddy kinetic energy model for simulations of the oceanic vertical mixing: Tests at station Papa and long-term upper ocean study site. J. Geophys. Res.: Oceans **95**: 16179–16193. doi:10.1029/JC095iC09p16179

Giovanoli, F. 1990. Horizontal transport and sedimentation by interflows and turbidity currents in Lake Geneva. In Large lakes: Ecological structure and function, ed. by M. M. Tilzer and C. Serruya, 175–195. Springer.

Goldscheider, N., L. Haller, J. Poté, W. Wildi, and J. Zopfi. 2007. Characterizing water circulation and contaminant transport in Lake Geneva using bacteriophage tracer experiments and limnological methods. Environ. Sci. Technol. **41**: 5252–5258. doi:10.1021/es070369p

Halder, J., L. Decrouy, and T. W. Vennemann. 2013. Mixing of Rhône River water in Lake Geneva (Switzerland-France) inferred from stable hydrogen and oxygen isotope profiles. J. Hydrol. **477**: 152–164. doi:10.1016/j.jhydrol.2012.11.026

Hannachi, A., I. T. Jolliffe, and D. B. Stephenson. 2007. Empirical orthogonal functions and related techniques in atmospheric science: A review. Int. J. Climatol. **27**: 1119–1152. doi:10.1002/joc.1499

Hill, C., D. Ferreira, J.-M. Campin, J. Marshall, R. Abernathey, and N. Barrier. 2012. Controlling spurious diapycnal mixing in eddy-resolving height-coordinate ocean models - insights from virtual deliberate tracer release experiments. Ocean Model. **45-46**: 14–26. doi:10.1016/j.ocemod.2011.12.001

Ishiguro, N. 2004. L'influence du climat et des affluentes sur l'oxygénation et la turbidité des lacs: le cas comparé du Léman, des lacs alpins et japonais. Ph.D. thesis. Université de Limoges, France.

Jarvis, A., H. I. Reuter, A. Nelson and E. Guevara. 2008. Hole-filled seamless SRTM data V4. International Centre for Tropical Agriculture (CIAT). [accessed 2018 May 25]. Available from http://srtm.csi.cgiar.org.

LaCasce, J. H. 2008. Statistics from Lagrangian observations. Progr. Oceanogr. **77**: 1–29. doi:10.1016/j.pocean.2008.02.002

Legler, D. M. 1983. Empirical orthogonal function analysis of wind vectors over the tropical Pacific region. Bull. Am. Meteorol. Soc. **64**: 234–241. doi:10.1175/1520-0477(1983)064<0234:EOFAOW>2.0.CO;2

Lemmin, U., and N. D'Adamo. 1997. Summertime winds and direct cyclonic circulation: Observations from Lake Geneva. Ann. Geophys. **14**: 1207–1220. doi:10.1007/s00585-996-1207-z

Lemmin, U., C. H. Mortimer, and E. Bäuerle. 2005. Internal seiche dynamics in Lake Geneva. Limnol. Oceanogr. **50**: 207–216. doi:10.4319/lo.2005.50.1.0207

Loizeau, J.-L., S. Girardclos, and J. Dominik. 2012. Taux d'accumulation de sédiments récents et bilan de la matière particulaire dans le Léman (Suisse-France). Arch. Sci. **65**: 81–92.

Loizeau, J.-L., S. Marki, P. Appagaus, B. Ferrari, C. Casaso-Martinez, T. Benejam, and P. Marchand. 2017. Micropolluants métalliques et organiques dans les sédiments superficiels du Léman 2015. Rapp. CIPEL, Campagne; 143–158.

Marshall, J., A. Adcroft, C. Hill, L. Perelman, and C. Heisey. 1997. A finite-volume, incompressible Navier Stokes model for studies of the ocean on parallel computers. J. Geophys. Res.: Oceans **102**: 5753–5766. doi:10.1029/96JC02775.

Mercanton, P. L. 1932. Etude de la circulation des eaux du Lac Léman. Mém. Soc. Vaudoise Sci. Nat. **4**: 225–271.

Monsen, N. E., J. E. Cloern, L. V. Lucas, and S. G. Monismith. 2002. A comment on the use of flushing time, residence time, and age as transport time scales. Limnol. Oceanogr. **47**: 1545–1553. doi:10.4319/lo.2002.47.5.1545

Percival, D. B., and A. T. Walden. 1993. Spectral analysis for physical applications. Cambridge Univ. Press.

Razmi, A. M., D. A. Barry, U. Lemmin, F. Bonvin, T. Kohn, and R. Bakhtyar. 2014. Direct effects of dominant winds on residence and travel times in the wide and open lacustrine embayment: Vidy Bay (Lake Geneva, Switzerland). Aquat. Sci. **76**: 59–71. doi:10.1007/s00027-013-0321-8

Steinbuck, J. V., J. R. Koseff, A. Genin, M. T. Stacey, and S. G. Monismith. 2011. Horizontal dispersion of ocean tracers in internal wave shear. J. Geophys. Res.: Oceans **116**: C11031. doi:10.1029/2011JC007213

Stocker, R., and J. Imberger. 2003. Horizontal transport and dispersion in the surface layer of a medium-sized lake. Limnol. Oceanogr. **48**: 971–982. doi:10.4319/lo.2003.48.3.0971

Umlauf, L., and U. Lemmin. 2005. Interbasin exchange and mixing in the hypolimnion of a large lake: The role of long internal waves. Limnol. Oceanogr. **50**: 1601–1611. doi:10.4319/lo.2005.50.5.1601

Vernet, J.-P., and M. Viel. 1984. Metaux lourds dans les sédiments lacustres, p. 229–238. *In* Le Léman; Synthèse 1957–1982. CIPEL

von Storch, H., and F. W. Zwiers. 1999. Statistical analysis in climate research. Cambridge Univ. Press.

Voudouri, A., E. Avgoustoglou and P. Kaufmann. 2017. Impacts of observational data assimilation on operational forecasts. In Perspectives on atmospheric sciences, ed. by Karacostas T., Bais A. and Nastos P., 143–149. Springer, Cham, Switzerland.

## Acknowledgments

The authors thank P. Benettin for input concerning water age characterization. For providing field observations, the authors thank SOERE OLA-IS, INRA Thonon-les-Bains (France), developed by the Eco-Informatics ORE INRE Team. The authors also extend their thanks to the Federal Office of Meteorology and Climatology (MeteoSwiss) for COSMO data, the Canton Vaud (Switzerland) for the bathymetry data, and Jarvis et al. (2008) for the topographic data. The authors thank the reviewers for their constructive comments that helped improve the manuscript. We also acknowledge support of SNF grant 159422.

## Conflict of Interest

The authors are not aware of any conflict of interest.

*Submitted 08 March 2018*
*Revised 28 May 2018*
*Accepted 04 December 2018*

*Associate editor: Leon Boegman*